

## Rheology-based wall function approach for wall-bounded turbulent flows of Herschel–Bulkley fluids

Yusufi, B. K.; Kapelan, Z.; Mehta, D.

**DOI**

[10.1063/5.0180663](https://doi.org/10.1063/5.0180663)

**Publication date**

2024

**Document Version**

Final published version

**Published in**

Physics of Fluids

**Citation (APA)**

Yusufi, B. K., Kapelan, Z., & Mehta, D. (2024). Rheology-based wall function approach for wall-bounded turbulent flows of Herschel–Bulkley fluids. *Physics of Fluids*, 36(2), Article 023112. <https://doi.org/10.1063/5.0180663>

**Important note**

To cite this publication, please use the final published version (if applicable). Please check the document version above.

**Copyright**




Other than for strictly personal use, it is not permitted to download, forward or distribute the text or part of it, without the consent of the author(s) and/or copyright holder(s), unless the work is under an open content license such as Creative Commons.

**Takedown policy**

Please contact us and provide details if you believe this document breaches copyrights. We will remove access to the work immediately and investigate your claim.

RESEARCH ARTICLE | FEBRUARY 20 2024

# Rheology-based wall function approach for wall-bounded turbulent flows of Herschel–Bulkley fluids

B. K. Yusufi ; Z. Kapelan ; D. Mehta 

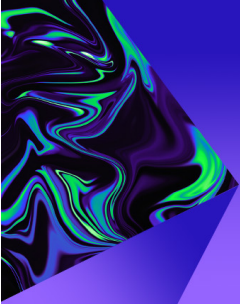


*Physics of Fluids* 36, 023112 (2024)

<https://doi.org/10.1063/5.0180663>




CrossMark



## Physics of Fluids

Special Topic:  
Selected Papers from the 2023 Non-Newtonian  
Fluid Mechanics Symposium in China

**Submit Today**



# Rheology-based wall function approach for wall-bounded turbulent flows of Herschel–Bulkley fluids

Cite as: Phys. Fluids **36**, 023112 (2024); doi: 10.1063/5.0180663

Submitted: 11 October 2023 · Accepted: 2 February 2024 ·

Published Online: 20 February 2024



View Online



Export Citation



CrossMark

B. K. Yusufi,<sup>a)</sup>  Z. Kapelan,  and D. Mehta 

## AFFILIATIONS

Department of Water Management, Faculty of Civil Engineering and Geosciences, Delft University of Technology, Delft 2628 CN, The Netherlands

<sup>a)</sup> Author to whom correspondence should be addressed: [b.k.yusufi@tudelft.nl](mailto:b.k.yusufi@tudelft.nl)

## ABSTRACT

Modeling fully developed turbulent flow for Herschel–Bulkley (HB) fluids in pipes is a long-standing challenge. Existing semi-empirical, theoretical, and numerical methods are either inconsistent with experimental data or are validated for low Reynolds numbers. This study focuses on validating a novel approach using rheology-based wall functions within Reynolds-averaged Navier–Stokes solvers. Simulations of wall shear stress and velocity profiles were conducted across a wide range of Reynolds numbers using a single-phase HB fluid, with measurements taken both upstream and downstream of a 90° pipe bend. Two turbulence closure models, the  $k$ – $\epsilon$  model and the Reynolds stress model, were employed with the wall function implemented as a specified shear boundary condition. Results demonstrate significant improvements over the Newtonian-based models, such as standard wall function by Launder–Spalding or with available semi-empirical models, achieving strong statistical correlations and minimal deviation (from the experimental findings) at high Reynolds numbers. The study also examines the utility of the wall viscosity Reynolds number and assesses the reliability of semi-empirical models for HB fluids. These findings offer valuable insights for enhancing modeling accuracy in complex fluid flow scenarios, with potential applications spanning industries like mining, chemical processing, petroleum transportation, and sanitation systems, providing practical alternatives to costly experimental procedures in pipe systems.

© 2024 Author(s). All article content, except where otherwise noted, is licensed under a Creative Commons Attribution (CC BY) license (<http://creativecommons.org/licenses/by/4.0/>). <https://doi.org/10.1063/5.0180663>

## I. INTRODUCTION

The modeling of turbulent non-Newtonian flows has a long history, dating back to 1959 with the pioneering work of Tomita,<sup>1</sup> who proposed a semi-empirical model using the Prandtl mixing length theory.<sup>2</sup> A turbulent flow of power-law (PL) and Bingham plastic (BP) fluids was assumed as an imaginary laminar flow with an average velocity equal to the turbulent flow velocity. Building on this, Dodge and Metzner<sup>3</sup> derived a semi-empirical correlation using Buckingham pi dimensional analysis<sup>4</sup> for fully developed turbulent flows with PL fluids. Furthermore, advancements were made by Torrance,<sup>5</sup> who modified the von Karman constant based on the fluid behavior index and incorporated the effect of pipe roughness, and by Wilson and Thomas,<sup>6,7</sup> who predicted drag reduction through the thickening of the laminar sub-layer due to enhanced viscosity near the wall region. Additionally, Slatter<sup>8</sup> conducted an extensive experimental investigation proposing semi-empirical velocity distributions for turbulent Herschel–Bulkley (HB) flows. This correlation resembled the logarithmic velocity profiles observed in Newtonian fluids.

Despite their contributions, these models are subject to certain limitations due to the underlying assumptions made in their formulation or due to the limited training data set. For instance, the validity of Tomita's model has not been established using independent experimental data despite being tested across a wide range of Reynolds numbers.<sup>9,10</sup> The Dodge and Metzner<sup>3</sup> approach provides a method for determining wall shear stress ( $\tau_w$ ) in non-Newtonian fluids by deriving apparent behavior ( $n'$ ) and consistency ( $m'$ ) indexes from a shear stress–shear rate curve. This process is straightforward for PL fluids with constant  $n'$  and  $m'$  values. However, it becomes more intricate for HB, as used in this article. In HB fluids, due to yield stress, the values of  $n'$  and  $m'$  are dependent on the unknown  $\tau_w$ . The procedure involves an initial assumption of  $\tau_w$  followed by an iterative approach to solve the Dodge and Metzner<sup>3</sup> correlation. Nevertheless, there are no established guidelines for accurately predicting or assuming the correct value of  $\tau_w$  beforehand.

Models proposed by Torrance<sup>5</sup> and Wilson and Thomas<sup>6,7</sup> were found to be accurate at the early stage of turbulence but were sensitive

to rheological parameters as reported by Slatter.<sup>8</sup> In Slatter’s model, certain assumptions, such as the impact of particles near the wall leading to a reduction in velocity gradient akin to pipe roughness and the utilization of the representative particle size ( $d_{gs}$ ), lack a solid theoretical foundation. Also, the assumption that the plug flow abruptly disappears at the critical Reynolds number during the transition from laminar to turbulent flow contradicts Bowen findings<sup>11</sup> and experimental observations by Peixinho *et al.*<sup>12</sup> Hence, to summarize, the inherent complexity of non-Newtonian fluids, combined with the limited understanding of turbulence in such fluids, significantly restricts the applicability of these semi-empirical models. As a result, significant disparities exist among the various models.<sup>13</sup> Nevertheless, due to their widespread usage and the absence of alternative methods, these models will be employed for comparative purposes in this article.

In addition to the existing semi-empirical approaches, theoretical methods were proposed, such as the one by Hanks<sup>14</sup> for HB fluids, aiming to establish a family of friction factor–Reynolds number curves akin to Moody’s chart. However, the approach lacks experimental validation and is also known to be time and resource-intensive. In recent years, numerical simulations of non-Newtonian turbulent flows have gained significant popularity in various industries, including mining, petroleum, chemical, paper-pulp, construction, and sanitation, to facilitate efficient material transportation through large diameter pipes.<sup>15,16</sup> These methods offer a cost and time-efficient solution, providing notable advantages over experimental methods, particularly for handling opaque fluids where conventional techniques like particle imaging velocimetry (PIV) are impractical.<sup>17</sup>

While several numerical simulation techniques, such as direct numerical simulations (DNS) and large eddy simulations (LES), have broad applicability, they are computationally expensive and have limitations in simulating turbulence beyond certain levels.<sup>18</sup> Striking a balance between computational cost and accuracy, the Reynolds-averaged Navier–Stokes (RANS) modeling approach emerges as the most suitable option.<sup>19</sup> However, despite its advantages, RANS modeling for highly turbulent flows of time-independent HB fluids has not received sufficient attention from the computational fluid dynamics (CFD) community. As a result, Newtonian models are still being used to describe non-Newtonian flows.<sup>20</sup>

The RANS approach solves the Navier–Stokes equation, but for non-Newtonian HB fluids, it presents challenges in closing three terms: Reynolds stresses, non-Newtonian molecular viscosity, and the fluctuating viscosity stress tensor; we will discuss this in more detail later in this section. To begin with, it is important to understand how turbulent HB fluids flow through pipes. This involves solving a set of equations that describe the continuity of the flow and the Navier–Stokes equations. Assuming the flow is incompressible, and gravity is the only body force, these equations can be expressed in Cartesian form as follows:

$$\frac{\partial u_i}{\partial x_i} = 0, \tag{1}$$

$$\rho \frac{\partial (u_i)}{\partial t} + \rho \frac{\partial (u_j u_i)}{\partial x_j} = -\frac{\partial p}{\partial x_i} + \frac{\partial \tau_{ij}}{\partial x_j} - \rho g. \tag{2}$$

Here,  $x_i$  ( $i = 1, 2, 3$ ) or  $(x, y, z)$  represent the Cartesian coordinates, while  $u_i$  or  $(u_x, u_y, u_z)$  are the Cartesian components of the velocity vector  $u$ . Additionally,  $\rho$  and  $p$  denote the fluid density and static pressure, respectively, while  $g$  is the constant gravitational

acceleration. The stress tensor  $\tau_{ij}$  is associated with the strain rate tensor ( $S_{ij}$ ) as follows:

$$\tau_{ij} = 2\mu S_{ij} \quad \text{and} \quad S_{ij} = \frac{1}{2} \left( \frac{\partial u_j}{\partial x_i} + \frac{\partial u_i}{\partial x_j} \right), \tag{3}$$

where  $\mu$  is the effective viscosity of the fluid and depends on the shear rate ( $\dot{\gamma}$ ) as follows:

$$\mu = \mu(\dot{\gamma}) \quad \text{and} \quad \dot{\gamma} = \sqrt{2S_{ij} \cdot S_{ij}}. \tag{4}$$

We decompose each quantity as a sum of its average and fluctuating components to solve the above equation using the RANS approach. Reynolds decomposition, for any variable  $\phi$ , can be written down as follows:

$$\phi(\mathbf{x}, t) = \overline{\phi}(\mathbf{x}) + \phi'(\mathbf{x}, t). \tag{5}$$

In RANS modeling, the turbulent scales are ensemble-averaged (meaning an average over many instances of the flow) to obtain a time-independent representation of the flow.<sup>21</sup>

$$\overline{\phi}(\mathbf{x}) = \lim_{T \rightarrow \infty} \frac{1}{T} \int_{t_0}^{t_0+T} \phi(\mathbf{x}, t) dt. \tag{6}$$

Now, applying Reynolds decomposition and time averaging to the above Navier–Stokes equations for Newtonian fluids, we get

$$\frac{\partial \overline{u}_i}{\partial x_i} = 0, \tag{7}$$

$$\rho \overline{u}_j \frac{\partial \overline{u}_i}{\partial x_j} = -\frac{\partial \overline{p}}{\partial x_j} + \frac{\partial}{\partial x_j} \left( \overline{\mu \dot{\gamma}_{ij}} - \rho \overline{u'_i u'_j} \right) - \rho g. \tag{8}$$

The above equation can be solved to obtain the ensemble average of velocity  $\overline{u}$  and pressure field  $\overline{p}$ . The above resultant RANS equations are true for Newtonian fluids with constant molecular viscosity. However, if the molecular viscosity is not constant but a function of shear rate (the case of a purely viscous non-Newtonian fluid), the resultant equation after Reynolds decomposition and ensemble averaging will have terms containing average ( $\overline{\eta}$ ) and fluctuating effective viscosity ( $\eta'$ ). Including these terms in Eq. (8), we get

$$\rho \overline{u}_j \frac{\partial \overline{u}_i}{\partial x_j} = -\frac{\partial \overline{p}}{\partial x_j} + \frac{\partial}{\partial x_j} \left( \overline{\eta \dot{\gamma}_{ij}} - \rho \overline{u'_i u'_j} + \overline{\eta' \dot{\gamma}'_{ij}} \right) - \rho g. \tag{9}$$

To close Eq. (8), closure for the Reynolds stress term  $-\rho \overline{u'_i u'_j}$  is required. Boussinesq approximated the Reynolds stresses in terms of mean strain rate as follows:

$$\tau_{ij} = \mu_t \left( \frac{\partial \overline{u}_i}{\partial x_j} + \frac{\partial \overline{u}_j}{\partial x_i} \right), \tag{10}$$

where  $\mu_t$  is the eddy viscosity.

Since the average velocities are known, it is now required to determine the value of  $\mu_t$ . Various models are available to determine  $\mu_t$  based on the number of transport equations used in addition to momentum equations, such as the zero-equation model,<sup>2</sup> one-equation models,<sup>22</sup> two-equation models, such as  $k$ – $\epsilon$  model<sup>23</sup> and  $k$ – $\omega$  model,<sup>24</sup> and the Reynolds stress model (RSM).<sup>25</sup> For details, readers are recommended to refer to Wilcox.<sup>26</sup> To solve Eq. (9), in

addition to modeling Reynolds stresses and expressing non-Newtonian molecular viscosity, one also needs closure for the  $\eta'\gamma'_{ij}$  term, called the fluctuating viscosity stress tensor. Researchers in the literature have attempted to close these terms using different approaches.

While modified low Reynolds number  $k-\epsilon$  turbulence models have been used to determine the friction factor for HB fluids such as by Malin<sup>27–29</sup> and Bartosik,<sup>30</sup> they rely on the damping function hypothesis and local values, lacking differentiation between viscous and non-viscous damping effects. Low Reynolds number  $k-\epsilon$  models for generalized Newtonian fluids have been developed by Pinho and Cruz<sup>18,31</sup> and validated for at low Reynolds numbers PL fluids.<sup>32</sup> Also, the authors assumed isotropic turbulence, which can be true for Newtonian fluids, but non-Newtonian fluids show a high level of anisotropy. Thus, the applicability of such models for highly non-Newtonian fluids at a high Reynolds number has not been established. To address these limitations, Gavrilov and Rudyak<sup>33,34</sup> attempted to incorporate anisotropic turbulence and account for viscosity fluctuations for PL fluids using an elliptical relaxation function. Lovato *et al.*<sup>20</sup> extended this work to HB fluids but highlighted the need for further experimental validation.

Another approach involves employing a semi-empirical velocity distribution as a wall function in CFD solvers, as demonstrated by Sawko.<sup>35</sup> Sawko utilized semi-empirical models by Dodge and Metzner<sup>3</sup> and Clapp<sup>36</sup> (described below). In the case of non-Newtonian fluids, the logarithmic law of the wall can be described as follows:

$$u^+ = A \ln y^+ + B, \tag{11}$$

where  $u^+$  and  $y^+$  are non-dimensional velocity and distance from the wall and are given by

$$u^+ = \frac{u}{u_\tau}, \tag{12}$$

$$y^+ = \frac{\rho y u_\tau}{\mu}, \tag{13}$$

and  $u_\tau$  is shear velocity defined as follows:

$$u_\tau = \sqrt{\frac{\tau_w}{\rho}}. \tag{14}$$

$A$  and  $B$  are coefficients derived from experimental data. Dodge and Metzner<sup>3</sup> defined these coefficients as follows:

$$A = \frac{5.66}{n^{0.75} \ln 10}, \tag{15}$$

$$B = -\frac{0.4}{n^{0.75}} + \frac{2.458}{n^{0.75}} \left[ 1.96 + 1.255n - 1.628n \log \left( 3 + \frac{1}{n} \right) \right]. \tag{16}$$

For Clapp, these coefficients are

$$A = \frac{2.78}{n} \quad \text{and} \quad B = \frac{3.8}{n}. \tag{17}$$

Extending Clapp's approach to HB fluids, Mehta *et al.*<sup>37</sup> derived a relationship between fluid velocity and wall shear stress near the wall. This relationship was implemented in CFD solvers as a specified shear boundary condition, and we will delve into this approach in the subsequent section. However, despite its validation for wall shear stress using various datasets, validation for other parameters, such as velocity profiles, remains incomplete.

This article aims to address this gap by evaluating the performance of the rheology-based wall function approach (proposed in Mehta *et al.*<sup>37</sup>) in terms of wall shear stress and velocity profiles. The obtained results will be compared with experimental data presented by Dash,<sup>38</sup> the Newtonian-based wall function, and with well-established semi-empirical models available in the literature, namely, Dodge and Metzner,<sup>3</sup> Torrance,<sup>5</sup> Thomas and Wilson,<sup>7</sup> and Slatter.<sup>8</sup> Beyond validation and comparative analysis, this study also examines the utility of the wall viscosity Reynolds number in non-Newtonian fluid flows and assesses the reliability of semi-empirical approaches and the applicability of the pseudo-homogeneous assumption, thus providing valuable insights for improving modeling accuracy in complex fluid flow scenarios.

The rest of the paper is organized as follows. In Sec. II, the methodology employed in this study is presented. Section III provides details of the experimental setup and procedures employed for data collection. The results and discussion are presented in Sec. IV, focusing on wall shear stress, velocity profiles, and quantitative comparisons. Finally, in Sec. V, a summary of the main findings and conclusions drawn from this research is provided.

## II. METHODOLOGY

### A. Rheological classification

Herschel–Bulkley fluids exhibit a yield pseudo-plastic behavior characterized by a minimum stress requirement, known as yield stress, for flow to occur. These fluids display a shear-thinning nature, where the viscosity decreases with increasing shear rate. Figure 1 shows a typical representation of HB fluids on a shear stress-shear rate plot (called a rheogram) compared to Newtonian, PL, and BP fluids.

The expression for HB fluids was proposed by Herschel and Bulkley<sup>39</sup> typically given by the following equation, where  $\tau_y$  represents the yield stress,  $m$  is the consistency index, and  $n$  is the behavior index:

$$\tau = \tau_y + m\dot{\gamma}^n. \tag{18}$$

Equation (18) is applicable when the magnitude of the stress ( $|\tau|$  or  $\tau$ ) is greater than or equal to the yield stress ( $\tau_y$ ), typically  $|\tau| \geq \tau_y$ .

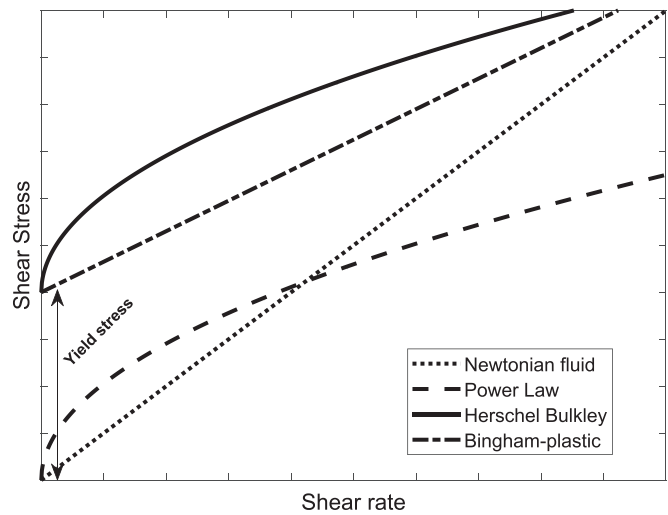


FIG. 1. Types of time-independent flow behavior.

When  $|\tau| < \tau_y$ , the shear rate ( $\dot{\gamma}$ ) is equal to zero. Also, this equation can be treated as a generalized equation for all purely viscous time-independent non-Newtonian fluids and reverts back to BP fluid for  $n = 1$ , PL fluid for  $\tau_y = 0$ , and Newtonian fluid for  $\tau_y = 0, n = 1$ , and  $m = \mu$ .

In three dimensions with full tensor notation (as in Oldroyd<sup>40</sup>), Eq. (18) reads

$$\tau = \left( \frac{\tau_y}{|\dot{\gamma}|} + m\dot{\gamma}^{n-1} \right) \dot{\gamma}, \tag{19}$$

where  $|\dot{\gamma}|$  is the second invariant of  $\dot{\gamma}$  and can be expressed as follows:

$$|\dot{\gamma}| = \sqrt{\frac{1}{2} \{\dot{\gamma} : \dot{\gamma}\}}, \tag{20}$$

$$\dot{\gamma} : \dot{\gamma} = \text{tr}(\dot{\gamma}^T \dot{\gamma}). \tag{21}$$

$\dot{\gamma} : \dot{\gamma}$  is the Frobenius product of  $\dot{\gamma}$ , tr is the trace of a square matrix that is the sum of its diagonal elements, and  $T$  is the transpose of the matrix.

Characterized by their shear rate-dependent viscosity, non-Newtonian fluid flows pose a challenge when described by conventional Reynolds number expressions. To address this, Rudman *et al.*<sup>41</sup> proposed a Reynolds number ( $Re_w$ ) based on wall viscosity. This approach differs from that proposed in Metzner and Reed<sup>42</sup> as it takes into account the influence of wall shear stress ( $\tau_w$ ) on the near-wall viscosity ( $\eta_w$ ), a critical factor shaping the turbulence characteristics of wall-bounded flows. By incorporating the wall viscosity, one can accurately capture the flow behavior near the wall and obtain more precise turbulent flow predictions in non-Newtonian fluids. Mathematically, we define  $Re_w$  as follows:

$$Re_w = \frac{\rho U D}{\eta_w}. \tag{22}$$

Here,  $\rho$  denotes fluid density,  $U$  represents cross-section averaged velocity, and  $D$  is inner pipe diameter. For HB fluids,  $\eta_w$  takes the form as follows:

$$\eta_w = m^{1/n} \frac{\tau_w}{(\tau_w - \tau_y)^{1/n}}. \tag{23}$$

Throughout this article, we adopt this definition of the Reynolds number.

### B. Wall function approach

Turbulent flows are characterized by sharp velocity, turbulent kinetic energy, and dissipation rate gradients near the wall. Capturing such steep gradients can be achieved by either resolving the near-wall region down to the viscous sub-layer ( $y^+ < 5$ ) or by using nonlinear wall functions.<sup>43</sup> In the first approach, for cases with high Reynolds numbers, the cells near the wall should be extremely small to resolve the flow in the viscous sub-layer. Additionally, when the wall is curved, such as in the case of flow in pipes (as in our study), the cells near the wall can become highly distorted unless the grid is significantly refined in the tangential direction. This increases computational costs and degrades mesh quality due to high aspect ratios.<sup>44</sup>

In the second approach, the first computational point is placed within the logarithmic region of the velocity profile ( $y^+ > 30$ ), and a relationship is established between the velocity at that point and the wall shear stress. This relationship is referred to as a wall function.<sup>26</sup> As a result, the required mesh resolution is significantly reduced, as illustrated in Fig. 2. Therefore, for flows with high-turbulence levels, employing a wall function is a more practical choice.

A commonly used wall function for Newtonian fluids, also termed as standard wall function in many CFD codes, was proposed by Launder and Spalding<sup>23</sup> and is given by

$$\frac{u}{(\tau_w/\rho)^{1/2}} = \frac{1}{\kappa} \ln \left\{ \frac{y\rho E}{\mu} \left( \frac{\tau_w}{\rho} \right)^{1/2} \right\}. \tag{24}$$

Here,  $\kappa$  is approximately 0.41 (the von Karman constant),  $y$  represents the distance from the pipe wall,  $\mu$  is dynamic viscosity, and  $E$  is a constant equal to 9.793.

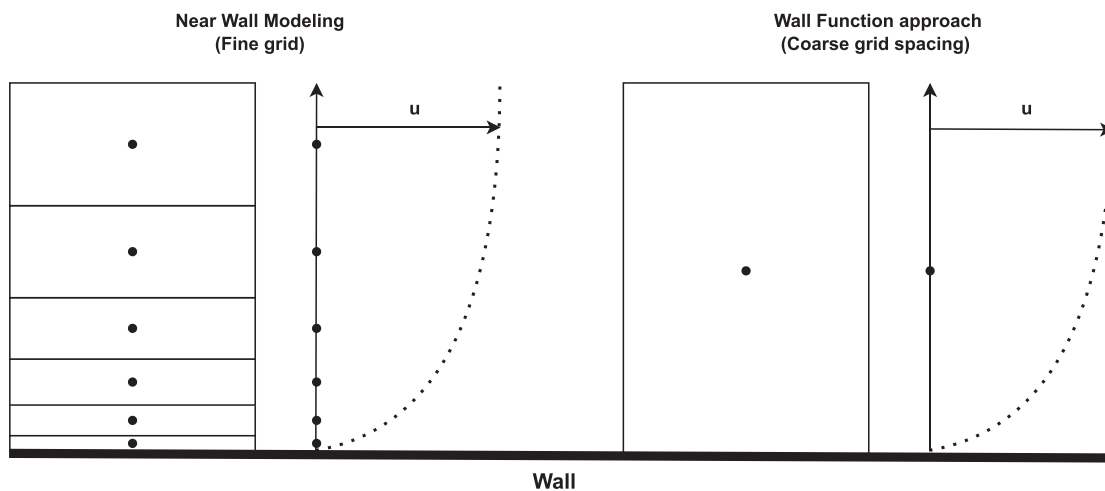
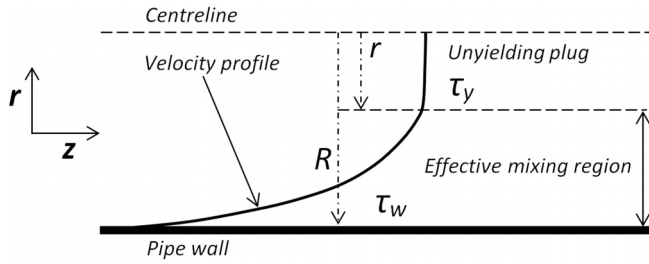


FIG. 2. Near-wall modeling vs wall function: implementing a wall function significantly reduces computational costs.



**FIG. 3.** Effective mixing region in a pipe conveying Herschel–Bulkley (HB) fluid. Image adapted from D. Mehta *et al.*, “A wall boundary condition for the simulation of a turbulent non-Newtonian domestic slurry in pipes,” *Water* **10**, 124 (2018). Copyright 2018 Authors, licensed under a Creative Commons Attribution (CC BY) license.

Mehta *et al.*<sup>37</sup> revised this model for HB fluids, resulting in the final expression of the wall function as follows:

$$\frac{u}{\left(\frac{\tau_w - \tau_y}{\rho}\right)^{\frac{1}{2}}} = \frac{1}{n\kappa} \ln \left\{ \underbrace{y^n \frac{\rho}{k} E \left(\frac{\tau_w - \tau_y}{\rho}\right)^{\frac{2-n}{2}}}_{\psi_1} \right\}. \quad (25)$$

Referring to Fig. 3 and incorporating the new mixing length into the equation due to the presence of yield stress, we obtain

$$\frac{u}{\left(\frac{\tau_w - \tau_y}{\rho}\right)^{\frac{1}{2}}} = \left(\frac{1}{1 - \zeta}\right) \frac{1}{n\kappa} \ln \left\{ \underbrace{y^n \frac{\rho}{k} E \left(\frac{\tau_w - \tau_y}{\rho}\right)^{\frac{2-n}{2}}}_{\psi_2} \right\}, \quad (26)$$

where  $\zeta$  is defined as follows:

$$\zeta = \frac{\tau_y}{\tau_w}. \quad (27)$$

$\psi_1$  and  $\psi_2$  are the wall functions based on fluid rheological parameters and are implicit in  $\tau_w$ . Thus, unlike the standard wall function,  $\psi_1$  and  $\psi_2$  will be implemented as a specified shear boundary condition. It is worth mentioning that the implementation of  $\psi_1$  is appropriate when the yield stress is insignificant compared to the wall shear stress. In contrast,  $\psi_2$  is applied when the yield stress is comparable to the wall shear stress. This was further discussed in a subsequent publication by Mehta *et al.*,<sup>45</sup> where an operational envelope was proposed to recommend the use of  $\psi_2$  when the ratio of wall shear stress to yield stress is less than ten; otherwise,  $\psi_1$  is recommended.

### C. Operational grid

The pipe geometry was discretized using ICEM-CFD. The first cell height was determined based on the  $y^+$  value calculated using Eq. (28), refer to Mehta *et al.*<sup>37</sup> for the derivation of the expression,

$$y^+ = \frac{y^n \cdot \rho}{k} \left(\frac{\tau_w - \tau_y}{\rho}\right)^{2-n/2}. \quad (28)$$

In all cases,  $y^+$  was maintained between 60 and 200 to ensure the mesh was confined to the log-law region. The cell height increased with a

growth factor of 1.05 as the distance from the wall increased. This standard practice is used in conjunction with wall functions for simulating turbulent boundary layers. In all cases, the grid followed the same pattern from the wall to half of the pipe radius, after which the cells were arranged more uniformly in an O-grid pattern, resulting in a total of 422 416 elements. To ensure the consistency of the mesh, a grid independence test was conducted, and finally, the numerical model was verified against the laminar analytical solution, with HB as the test fluid, as illustrated in Fig. 4.

### D. Solver

The CFD solver in this study is ANSYS Fluent (version 2021-R2), which employs the finite-volume method to solve the RANS equation discussed earlier. The fluid under consideration is a single-phase pseudo-homogeneous non-Newtonian HB fluid. The eddy viscosity models employ the  $k-\epsilon$  and RSM with standard model constants. The  $k-\omega$  model was not used due to its high computational cost. The inlet boundary conditions are set for flow velocity and turbulence. Turbulence specifications are based on hydraulic diameter and turbulent intensity, calculated using Eq. (29)<sup>46</sup> as shown as follows:

$$I = 0.16(Re_w)^{-\frac{1}{4}}. \quad (29)$$

Initially, a no-slip condition is applied at the pipe walls, which is then replaced with the specified shear once the solution reaches stability. As the outlet of the pipe loop is connected to a pipe that returns the fluid to the slurry reservoir (see Fig. 6), it is appropriate to use an outflow boundary condition at the outlet. The SIMPLE pressure-velocity coupling scheme is employed initially, which is subsequently replaced with COUPLED to ensure the stability of the simulation.<sup>46</sup> A second-order upwind scheme is used for spatial discretization to ensure numerical stability. The initial solution was established using hybrid initialization. Under-relaxation factors for pressure, momentum, turbulent kinetic energy, and turbulent dissipation rate were set at 0.5, 0.5, 0.75, and 0.75, respectively, while maintaining factors of one for density, body forces, and turbulent viscosity. Convergence for continuity, velocity,  $k$ , and  $\epsilon$  is attained through two criteria: first, employing relatively low residuals of  $10^{-9}$ , and second, ensuring sufficiently small solution imbalances, as depicted in Fig. 5. It has to be noted that the effect of temperature change has been neglected, assuming the isothermal conditions. Also, the pipe considered here is smooth; hence, any pipe roughness effects have not been incorporated.

### E. Simulations

In our simulations, we initially employ the standard wall function.<sup>23</sup> As the simulation progresses and approaches a steady-state solution, we transition to either  $\psi_1$  or  $\psi_2$ . During this process, theoretical constraints are imposed on the velocity field and wall shear stress, ensuring that the simulated flow field and shear stress adhere to the physical properties of the modeled HB fluid.

Starting with a uniform velocity field equivalent to the average flow velocity in the pipe, the simulation should converge onto a solution that satisfies either  $\psi_1$  or  $\psi_2$  near the wall for HB fluids. This is equivalent to using the original wall function for a Newtonian fluid. The wall function is expected to provide an accurate flow velocity profile with distance from the wall.

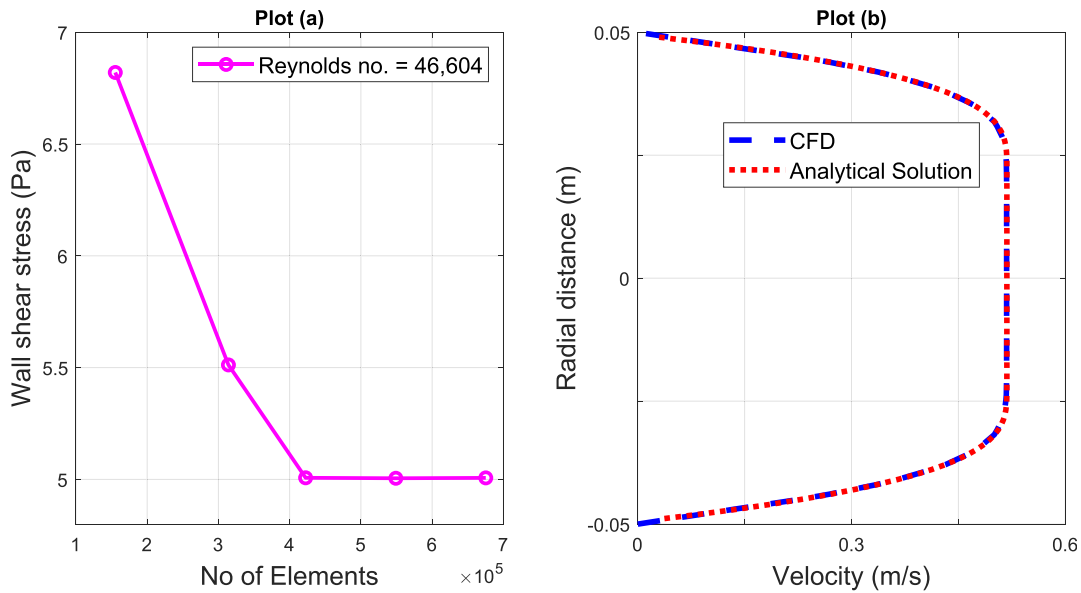


FIG. 4. For a fully developed flow at the horizontal section of the pipe: (a) grid-independency test at turbulent flow conditions and (b) verification of numerical model with the laminar analytical solution for Herschel–Bulkley fluids.

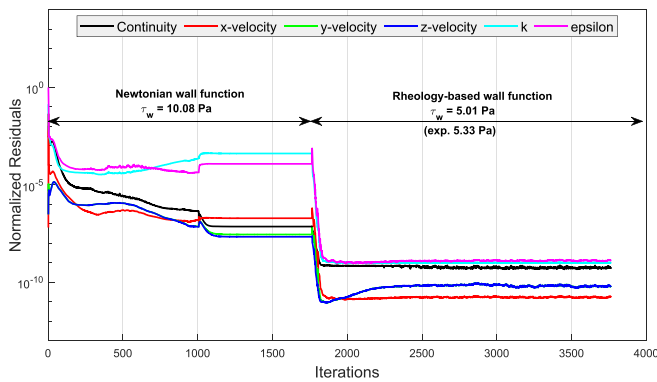


FIG. 5. Normalized residuals for test Case B ( $Re_w = 46\,604$ ). Applying the rheology-based wall function ( $\psi_1$ ) improved the numerical prediction of the wall shear stress.

### III. EXPERIMENTAL SETUP AND PROCEDURES

Experimental data were obtained from Dash,<sup>38,47,48</sup> where a kaolin–water mixture (21% w/w or 9% v/v) was used as the test fluid. This mixture demonstrated non-Newtonian behavior, characterized using the HB model detailed in Sec. II A and consistent with findings by Thota Radhakrishnan.<sup>49</sup> Rheological analysis was conducted using a HAAKE MARS I rheometer from Thermo Scientific, Germany, equipped with a conventional bob-cup geometry. Estimation of rheological parameters through Herschel–Bulkley modeling revealed an absolute normalized residual of 2% and a root mean square normalized residual of 3%. The rheological parameters of the tested slurry are presented in Table I.

TABLE I. Rheological characteristics of the experimental slurry (Ref. 38).

Parameter	Value
Mass density	1152.1 kg/m <sup>3</sup>
Yield stress ( $\tau_y$ )	0.8889 Pa
Behavior index ( $n$ )	0.4579
Consistency index ( $m$ )	0.1579 Pa s <sup><math>n</math></sup>
Pipe diameter	0.1 m

The tested slurry is composed of a single phase with a median particle size of 5.18  $\mu\text{m}$ . Considering the threshold particle size of 40  $\mu\text{m}$  for non-settling slurries flowing under industrially relevant velocities, this slurry can be considered pseudo-homogeneous.<sup>50</sup> The temperature was regulated at 18 °C with an accuracy of 0.1 °C through a Peltier system. Flow velocity and pressure changes were assessed with an electromagnetic flow meter (maximum error: 5%) and pressure transducers (maximum error: 2%), respectively. Figure 6 depicts the schematic of the experimental setup used in the  $\beta$ -loop.

Velocity profiles were obtained using ultrasound images recorded using an ultrasonic device coupled with linear transducers. The experimental campaign comprised eight cases with varying flow velocities, ranging from 0.55 ( $Re_w \approx 3500$ ) to 1.87 m/s ( $Re_w \approx 118\,000$ ), indicating the highly turbulent nature of the flow. The detailed information regarding the experimental parameters is tabulated in Table II. Velocity profiles were measured at eight different positions, with one upstream of the bend and the remaining seven downstream of the bend, as illustrated in Fig. 7. For the analysis, two positions, one upstream and one downstream of the bend, were considered since the velocity profiles remained consistent at the positions thereafter once



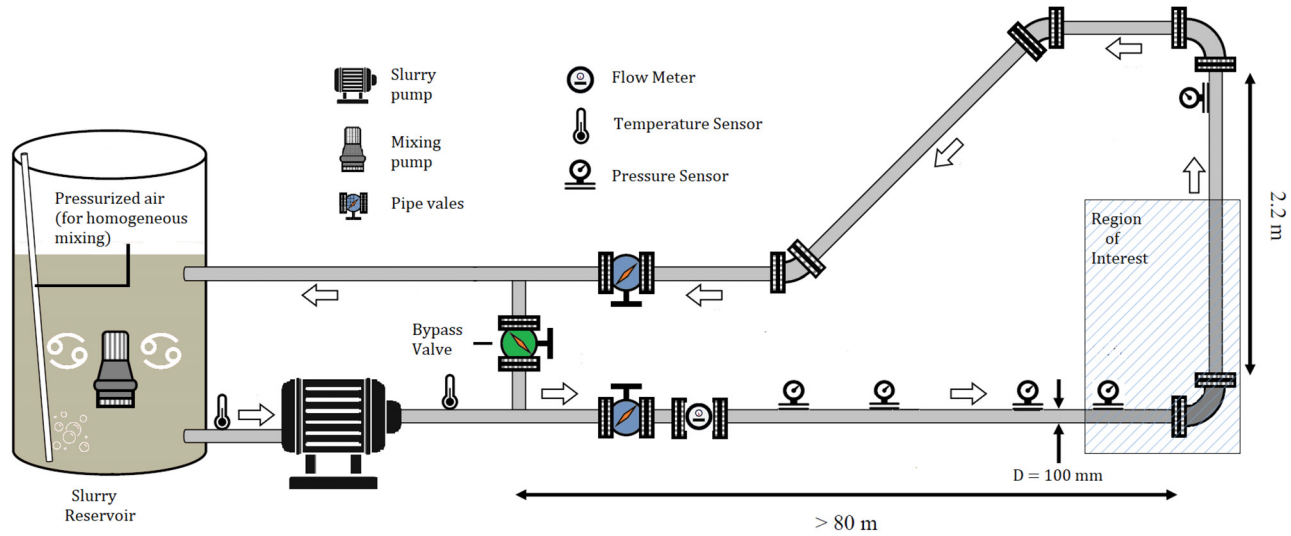


FIG. 6. Schematic of the experimental test facility ( $\beta$ -loop).

TABLE II. Experimental cases.

Cases	Velocities (m/s)	Wall shear stress (Pa)	Reynolds no. ( $Re_w$ )
A	1.875	8.378	117 896
B	1.477	5.329	46 604
C	1.308	4.230	27 956
D	1.174	3.501	17 709
E	0.984	2.649	8280
F	0.838	2.362	5366
G	0.798	2.204	4273
H	0.554	2.340	3463

the flow had fully developed. Furthermore, information on the experimental procedures can be found in Dash.<sup>38,48</sup>

IV. RESULTS AND DISCUSSION

A. Wall shear stress

We numerically have computed the wall shear stress (refer to Fig. 8) using both the  $k-\epsilon$  model and RSM with the standard wall function as well as the rheology-based wall functions,  $\psi_1$  or  $\psi_2$  (please note: the most accurate combination of  $\psi_1$  or  $\psi_2$  with either  $k-\epsilon$  model or RSM has been plotted). The results are compared with the experimental data and with the well-accepted Dodge and Metzner<sup>3</sup> semi-empirical model, modified for HB fluids by Reed and Pilehvari.<sup>51</sup>

Since non-Newtonian fluids exhibit complex flow behavior, it is unclear whether the flow is laminar or turbulent.<sup>9</sup> Therefore, we have also plotted the predictions of the laminar flow model (as shown in Fig. 8). To evaluate the accuracy of our simulations, we have incorporated error bars representing a 5% and 10% deviation from the experimental values.

One can observe that the wall shear stress predictions using the rheology-based wall function  $\psi_1$  (or  $\psi_2$ ) are within the 10% deviation

for most cases and within the 5% deviation at higher velocities, which represents a significant improvement over the standard wall function. Notably, the laminar model performs better than any other turbulent model up to a flow velocity of 0.98 m/s corresponding to a Reynolds number ( $Re_w$ ) of 8300. This could stem from the flow’s laminar nature at this stage, possibly explaining slight deviations of  $\psi_1$  (or  $\psi_2$ ) from experimental values.

This also casts doubt on the accuracy of the Reynolds number ( $Re_w$ ) and its relevance in accounting for wall viscosity. Although initial conditions heavily influence the exact point of transition, it is generally believed that the transition for non-Newtonian fluids occurs beyond a Reynolds number of 2100, roughly around 3000. This viewpoint finds support in an experimental study conducted by Escudier and Presti,<sup>52</sup> indicating that the transition behavior for HB fluids closely resembles that of Newtonian fluids. However, Fig. 8 illustrates the presence of laminar flow even at high Reynolds numbers, such as 8300. Consequently, relying solely on Reynolds numbers, particularly without accompanying experimental data to classify the flow, becomes less reliable. This highlights the necessity to consider  $Re_w$  alongside another dimensionless parameter (Hedstrom number<sup>53</sup>) akin to the approach adopted by Hanks.<sup>54</sup>

Interestingly, the Dodge and Metzner<sup>3</sup> model under-predicts the wall shear stress throughout the data range. This is consistent with the observations made by Sawko.<sup>35</sup> We hypothesize that this may be because the Dodge and Metzner<sup>3</sup> model was originally developed and calibrated using PL fluids that do not exhibit yield stress, unlike the HB fluid used in our study. As a result, modifying the Dodge and Metzner<sup>3</sup> model to account for the unique properties of HB fluids may not be feasible or accurate. These findings highlight the importance of using appropriate rheological models for different types of non-Newtonian fluids and caution against relying on models developed for one type of fluid to predict the behavior of another accurately.

Figure 9(a) compares the wall shear stress predictions obtained using the rheology-based wall functions,  $\psi_1$  and  $\psi_2$ . The ratio of wall

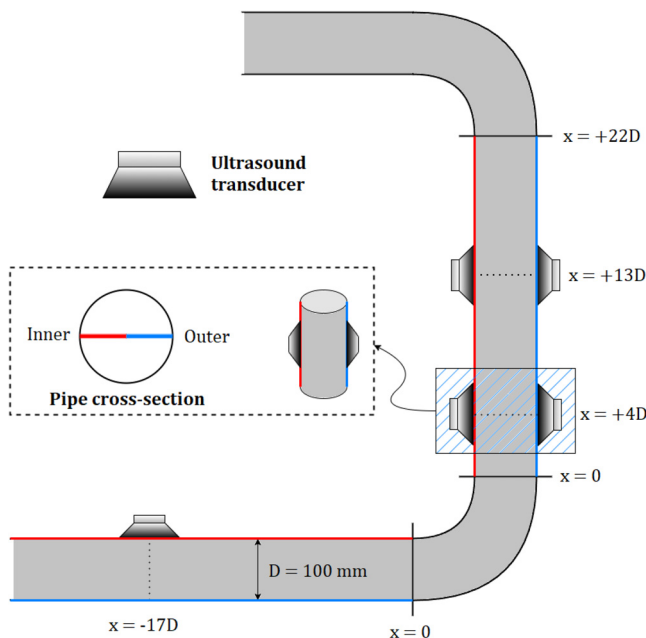


**FIG. 7.** Geometry illustrating a 90° pipe bend with measurements taken at locations upstream and downstream.

shear stress to yield stress ( $\tau_w/\tau_y$ ) for each case was less than 10. Contrary to the operational envelope proposed by Mehta *et al.*,<sup>45</sup> which suggests that  $\psi_2$  outperforms  $\psi_1$  when the yield stress is comparable to the wall shear stress (i.e.,  $\tau_w/\tau_y < 10$ ), we found  $\psi_1$  to be a better predictor of wall shear stress. However, as the ratio  $\tau_w/\tau_y$  decreased below four, both wall functions performed almost equally. This suggests that the proposed operational envelope may need revision with more experimental data.

In addition to comparing the performance of  $\psi_1$  and  $\psi_2$ , we also compared the predictions of the  $k-\epsilon$  model and RSM using a wall shear stress vs velocity plot, as shown in Fig. 9(b). Our results showed that the accuracy of the RSM increases as the flow becomes more turbulent. Specifically, we found that for the highest velocity, the accuracy of the RSM was much higher than that of the  $k-\epsilon$  model. This could be attributed to the fact that at such high-turbulence levels, the anisotropic formulation of the RSM is more suitable than the isotropic formulation of the  $k-\epsilon$  model. These findings are consistent with those reported by Mehta *et al.*<sup>37</sup>

### B. Velocity profile

In this section, we analyze the generated velocity profiles and compare them with the experimental data. The data consist of ultrasound-generated velocity profiles at eight locations, including one upstream of the 90° bend and seven downstream locations, discussed in Sec. III. The analysis focuses on one upstream location ( $x = -17D$ ) and one downstream location, as depicted in Fig. 7.

The flow through a pipe bend is a complex phenomenon marked by boundary layer separations, unsteadiness, turbulence, and the emergence of diverse secondary flows.<sup>55</sup> These flow characteristics influence not only the flow patterns downstream of the bend but also those upstream.<sup>56</sup> To minimize the influence of these secondary flows, selecting a location least

affected by them is crucial, especially when using well-known models developed for fully developed flows. Also, considering the potential vibrations near bends and joints caused by the change in fluid direction and resulting turbulence, selecting a location in the middle of the downstream region provides a more reliable and representative analysis.

Hence, the downstream location at a distance  $x = +13D$  was chosen based on the findings of Sudo *et al.*<sup>37</sup> Their work showed that approximately after a distance of  $10D$  downstream of the bend, the flow recovers its symmetrical profile with the breakdown of secondary motion. Hence, the generated velocity profiles were expected to be similar regardless of the downstream location. However, this general rule may vary depending on the bend curvature, fluid properties, and flow characteristics.

It is important to acknowledge that every experimental technique possesses its own set of capabilities and limitations. In this research, we rely on the data from Dash,<sup>38</sup> where ultrasound imaging velocimetry (UIV) has been employed to ascertain velocity profiles using a medical ultrasound device. The application of UIV to slurry flow within pipes introduces a significant challenge, as the received acoustic energy by the transducers exhibits substantial variation due to attenuation (resulting from absorption and/or scattering of sound) as the imaging depth changes. Enhancing accuracy demands the adoption of higher frequencies and specialized velocity measurement tools, such as ultrasonic velocity profilers (UVP), equipped with transducers.

Consequently, our primary focus in this study centers on aligning velocity profiles near the pipe wall, where experimental data are highly reliable. Therefore, our main interest lies in the shaded region in Figs. 10–12. This approach is consistent with the findings of Dodge and Metzner,<sup>3</sup> who demonstrated that the majority of mean velocity contributions occur in the immediate vicinity of the pipe wall, characterized by a relative radial distance  $r/R > 0.8$ . In contrast, the region around the pipe’s center, where  $r/R < 0.8$ , contributes only a mere 7% of the total mean velocity contributions. To non-dimensionalize these plots, we have depicted the stream-wise velocity ( $u$ ) at a distance  $r$  from the pipe center in relation to the average flow velocity ( $U$ ). This is plotted against the relative distance from the pipe center ( $r/R$ ), with  $R$  representing the pipe radius.

### 1. Upstream of 90° bend

Figure 11 presents a comparison between the velocity profiles generated from experimental data and CFD predictions, using  $\psi_1$  (or  $\psi_2$ ), at a distance of  $17D$  upstream of the bend. To provide context, we also compared the CFD predictions with standard wall function results, laminar velocity profiles at lower Reynolds numbers, and semi-empirical velocity models available in the literature. However, to avoid cluttering the plot, we first plotted the semi-empirical model predictions alone and compared them with the experimental data, as shown in Fig. 10. We considered velocity models by Torrance,<sup>5</sup> Thomas and Wilson,<sup>7</sup> and Slatter,<sup>8</sup> which are discussed previously in Sec. I.

The results show that Torrance<sup>5</sup> and Thomas and Wilson<sup>7</sup> models accurately predict the velocity profiles at an early stage of turbulence but diverge from the experimental data at higher Reynolds numbers. This observation is consistent with Slatter’s findings.<sup>8</sup> As discussed previously, Wilson and Thomas<sup>6,7</sup> formulated their model based on the thickening of the laminar sub-layer, resulting in drag reduction and an increase in velocity. At lower velocities, these micro-eddies and laminar sub-layers play an important role in shaping the

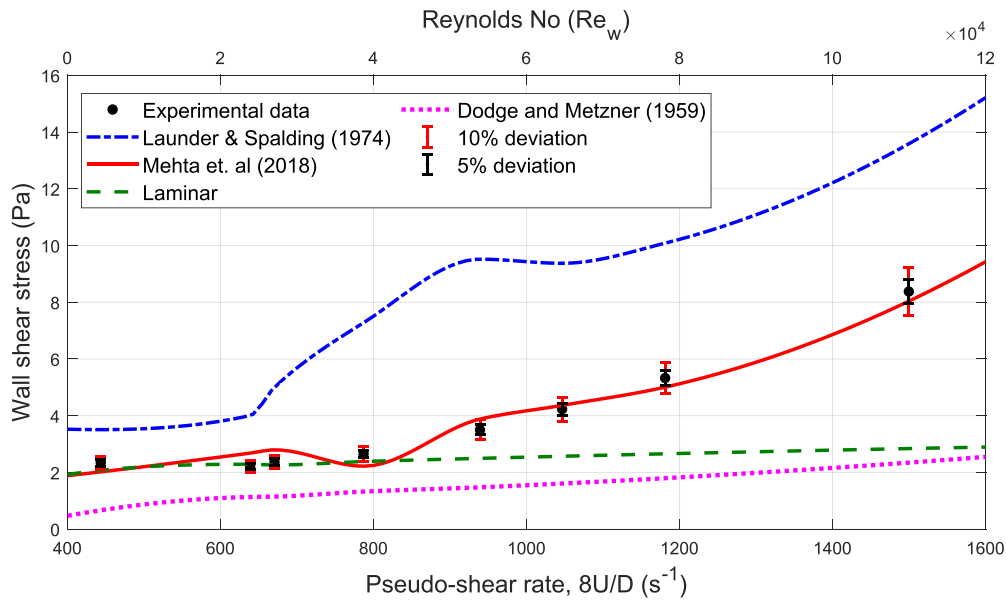


FIG. 8. Comparison of predicted wall shear stress from numerical models with experimental data.

velocity profiles, thus explaining why the model performs well in this region. However, at high turbulence, the laminar sub-layer becomes so thin that it can be of the order of particle sizes in the slurry, making it necessary to include particle size as a velocity function. This could be why Slatter’s model was most accurate in this region. Thus, we adopted Slater<sup>8</sup> for Cases A and B, Torrance<sup>5</sup> for Cases C and D, and Thomas and Wilson<sup>7</sup> for the rest of the cases.

Figure 11 shows that the rheology-based wall function provides an accurate match with experimental data for high Reynolds numbers ( $Re_w > 30\,000$ ) and becomes more accurate as the Reynolds number

increases (see Case A). This is because, at such high Reynolds numbers, the flow is governed primarily by turbulence viscosity, while molecular viscosity and its fluctuations are negligible, supporting the assumption of neglecting these terms.

However, for cases with  $Re_w < 30\,000$ , the predicted velocity profile deviates from the experimental data. This deviation increases as the flow rate decreases and laminar profiles become more accurate (see Case E). This discrepancy may arise due to the relevance of molecular viscosity, necessitating its consideration in the formulation. Consequently, all terms in Eq. (9) need to be modeled, as

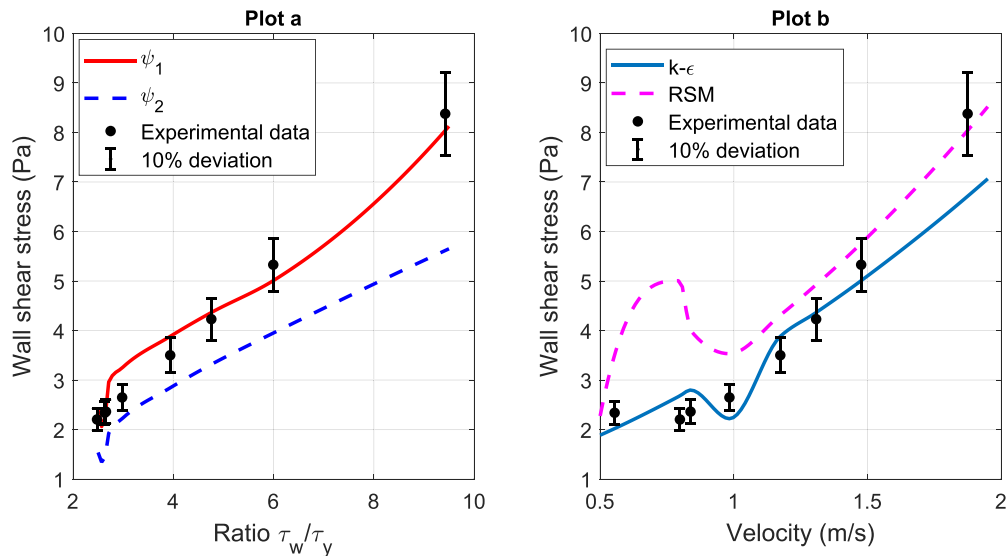


FIG. 9. (a) Comparison of  $\psi_1$  vs  $\psi_2$  and (b) comparison of  $k-\epsilon$  model vs RSM.

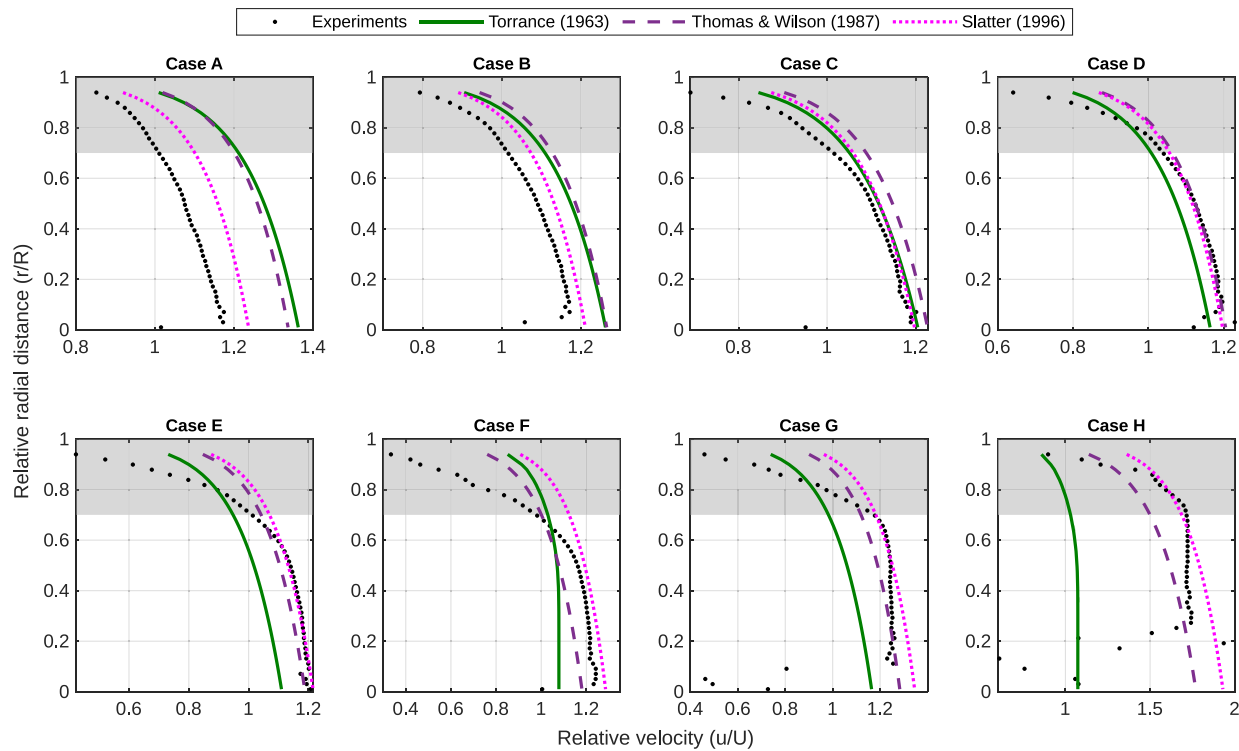


FIG. 10. Comparison of velocity profiles for the models available in the literature.

demonstrated in previous works by Gavrilov and Rudyak<sup>33</sup> and Lovato.<sup>20</sup> Additionally, as flow velocity decreases, more cells transition into the viscous region, characterized by a parabolic velocity profile. Therefore, the assumption of a logarithmic velocity profile in the wall function might not hold under these conditions. In such scenarios, a more prudent approach involves fully resolving the flow near the wall (with  $y^+$  close to one) using  $k-\omega$  models<sup>20</sup> or employing DNS,<sup>41</sup> albeit at a higher computational expense.

Another notable factor impacting velocity profile deviations at lower Reynolds numbers is particle settling, which initiates around a velocity of 0.99 m/s (Case E) and becomes more pronounced as the velocity decreases (Cases G and H), as reported by Dash and Poelma.<sup>48</sup> This causes dampening in the velocity profiles,<sup>58</sup> as can be seen from Fig. 11. In such scenarios, a prudent approach involves adopting a two-phase model, as suggested by Wasp.<sup>59</sup> This model accurately represents situations where settling becomes a dominant factor by capturing the transportation of solid particles (“payload”) within a carrier liquid (“vehicle”).

## 2. Downstream of 90° bend

Figure 12 presents a comparison of velocity profiles for different cases downstream of the bend. The radial coordinate  $r/R$  denotes the position within the pipe, where  $r/R = 1$  corresponds to the outer pipe wall and  $r/R = -1$  represents the inner pipe wall. It is noticeable that the  $\psi_1$  (or  $\psi_2$ ) profiles perform well for cases with higher Reynolds numbers but begin to diverge from the experimental profiles as flow

velocities decrease. These observations align with our earlier findings upstream of the bend at the  $-17 D$  location, discussed in Sec. IV B 1.

When comparing the results for upstream and downstream velocity profiles, it is evident that the predictions using  $\psi_1$  (or  $\psi_2$ ) are more accurate for downstream locations than upstream. This is because the presence of the bend induces secondary motions and increases turbulence in the fluid flow, eventually minimizing the settling of particles. Also, as these wall functions are derived for turbulent flows, it provides slightly better results for the downstream section (where the turbulence is comparatively more) than the upstream.

Additionally, it can be observed that the literature models tend to overpredict the velocity profiles in almost all cases, resulting in less flattened profiles. This indicates their inability to accurately capture the turbulence in the flow because of underlying assumptions and limitations, as discussed in Sec. I. It is also important to mention that these models failed to predict the zero-velocity gradient at the pipe center; however, this has a negligible effect on overall flow conservation.<sup>9</sup> Additionally, a depression can be noticed in the velocity profiles near the inner side of the pipe, which gradually diminishes as the Reynolds number increases. It is because inside the bend, the high-velocity fluid near the center of the pipe experiences centrifugal forces, resulting in outward movement, while slower-moving fluid particles near the pipe sides travel inward, creating counter-rotating Dean vortices.<sup>60</sup>

## C. Quantitative comparison

This section aims to provide a quantitative analysis of the wall function’s performance in predicting velocity profiles, comparing them

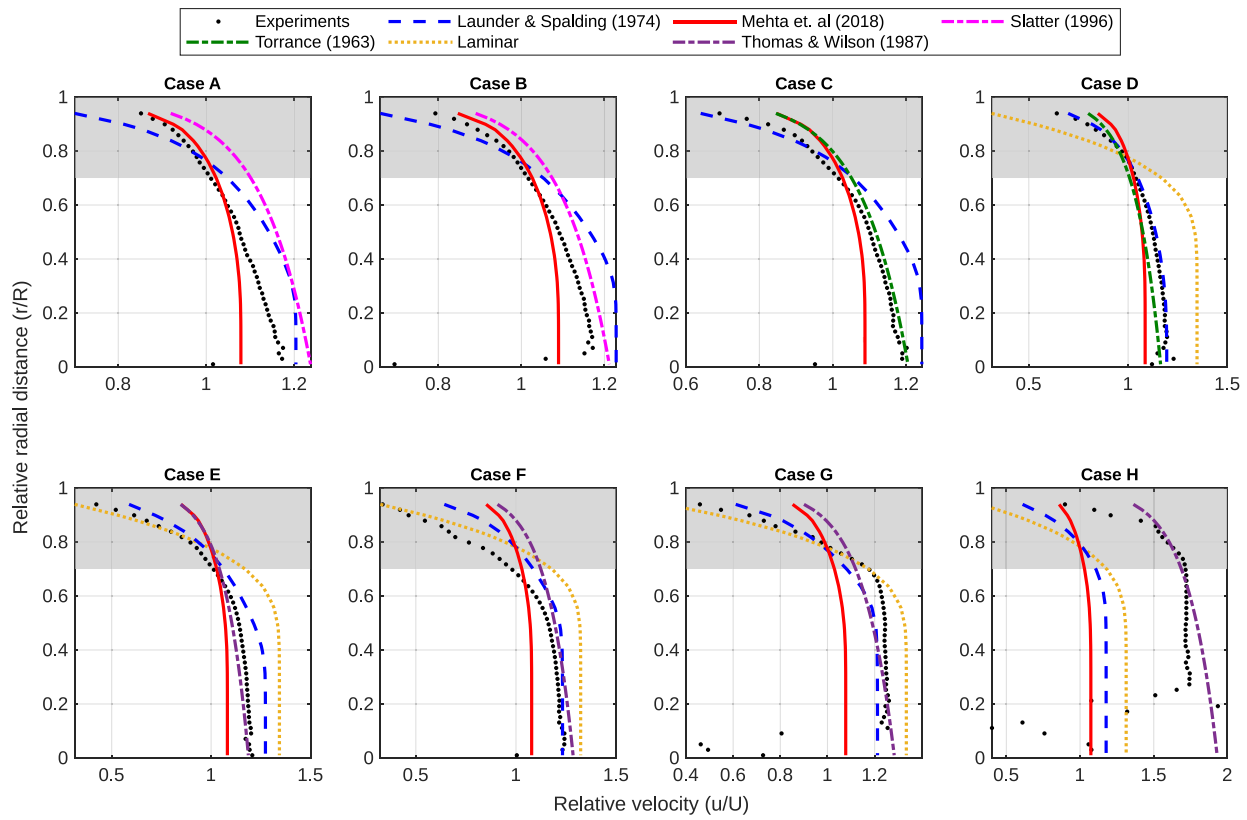


FIG. 11. Velocity profiles at 17 D upstream of bend.

against experimental data. It is worth noting that this comparison specifically focuses on profiles downstream of the bend, corresponding to the vertical section of the pipe. This choice of focus is grounded in our understanding that within this area, the influence of settling phenomena is at its lowest. To assess its accuracy, we will employ three evaluation metrics: root mean square error (RMSE), maximum error (ME), and the coefficient of correlation ( $R^2$ ). These statistical measures will allow us to evaluate the performance comprehensively. The obtained results are presented in Table III. Notably, implementing the rheology-based wall function approach significantly improves the predicted results. Specifically, the RMSE decreases from 0.148 (for the standard wall function) to 0.042. Likewise, the ME is reduced from 0.520 to 0.230 while achieving a correlation of 0.985. These findings highlight the enhanced accuracy and reliability of the rheology-based wall function approach in capturing the velocity profiles.

### V. CONCLUSION

In summary, this research evaluates the performance of a rheology-based wall function approach for Herschel–Bulkley fluids within a RANS solver, comparing predictions for wall shear stress and velocity profiles. Experimental data from a pipe loop study were utilized, where wall shear stress was computed using a pressure transducer, and velocity profiles were obtained through ultrasound imaging with a linear transducer. We also compared these predictions with conventional Newtonian-based models and established non-

Newtonian semi-empirical models across a wide range of flow conditions.

Our study underscores the critical significance of fluid rheology in turbulence modeling, especially when dealing with non-Newtonian fluids. Wall functions, when appropriately modified for these fluids, offer a practical way to account for rheological effects and improve the accuracy of predicting velocity profiles in turbulent flows. In conclusion, our key findings can be summarized as follows:

- The rheology-based wall functions ( $\psi_1$  and  $\psi_2$ ) significantly improve wall shear stress predictions, with deviations below 10% for most cases and below 5% for high Reynolds numbers when compared to standard wall functions and the established Dodge and Metzner<sup>3</sup> semi-empirical model. These findings align with Mehta *et al.*'s<sup>37</sup> conclusions.
- Velocity profiles are accurate in high-turbulence scenarios due to theoretical constraints imposed by  $\psi_1$  (or  $\psi_2$ ) near the wall. Deviations become more apparent as Reynolds numbers decrease, with the laminar model performing better. This discrepancy likely stems from two primary reasons: first, the exclusion of molecular viscosity and its fluctuations, and second, as flow velocity decreases, more cells transition into the laminar region, characterized by a parabolic velocity profile. Consequently, the assumption of a logarithmic velocity profile in the wall function may not hold in such cases.

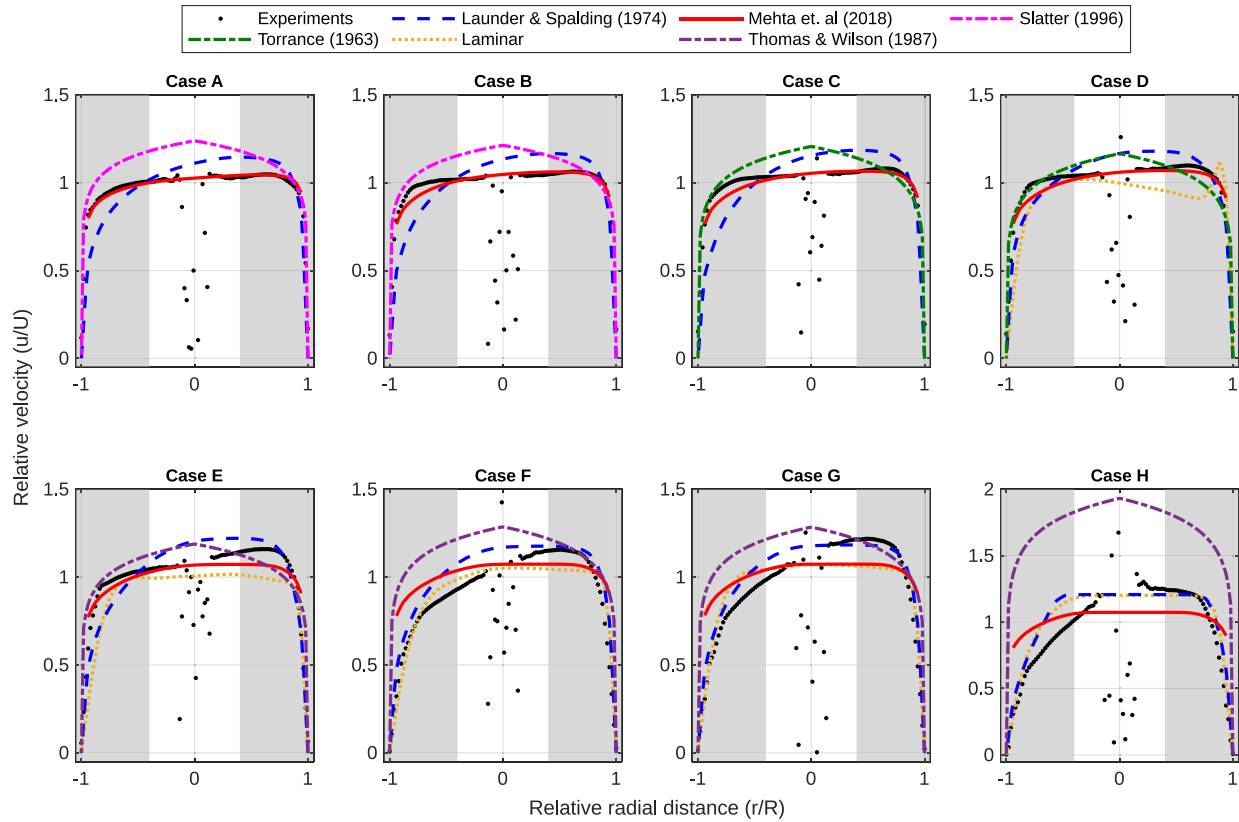


FIG. 12. Velocity profiles at 13 D downstream of bend.

- Despite the particles being smaller (with a representative size of  $5 \mu\text{m}$ ) than the critical settling size ( $40 \mu\text{m}$ ), the slurry still exhibited settling in the horizontal pipe section at lower velocities. Therefore, the assumption of a pseudo-homogeneous slurry requires careful consideration. While it holds for cases with higher Reynolds numbers, its applicability diminishes below the critical velocity, necessitating the adoption of a two-phase model when flow velocity falls below this threshold. Interestingly, downstream velocity profiles near bends exhibit better accuracy than upstream profiles, suggesting that the bend induces secondary motions, enhances turbulence, and promotes particle re-suspension.
- The wall viscosity Reynolds number ( $Re_w$ ) falls short in characterizing flow regimes for non-Newtonian fluids. Even at  $Re_w = 8300$ , laminar flow persists, challenging  $Re_w$  as a sole indicator. Additionally, the disparity between laminar wall shear stress and velocity profiles raises questions about relying solely on the Reynolds number. To enhance flow regime definition, introducing another dimensionless parameter, such as the Hedstrom number alongside the Reynolds number, may be necessary, similar to the approach by Hanks.<sup>54</sup> However, further experimental data are required to draw any definitive conclusions, which we plan to explore in our future research.
- The semi-empirical models prove inaccurate in predicting both wall shear stress and velocity profiles. The Dodge and Metzner<sup>3</sup> model consistently underestimates wall shear stress across all

Reynolds number ranges, while the Torrance,<sup>5</sup> Thomas and Wilson,<sup>7</sup> and Slatter<sup>8</sup> models consistently overpredict velocities. These discrepancies may stem from underlying assumptions, constraints due to limited experimental data, or a lack of universal applicability. A similar evaluation in Mehta *et al.*<sup>61</sup> found that the maximum probability of accurately predicting wall shear stress within a 95% confidence interval was only 0.27. This highlights the critical importance of careful model selection for precise predictions.

- Observations indicate that  $\psi_1$  generally outperforms  $\psi_2$  in most cases, even when the ratio  $(\tau_w/\tau_y)$  is below ten, which contrasts with Mehta *et al.*'s proposed operational envelope.<sup>45</sup> Consequently, the suggested operational envelope requires revision, supported by additional experimental data. Furthermore, in instances of highly turbulent flows ( $Re_w > 10\,000$ ), the flow

TABLE III. Quantitative comparison of different velocity models.

Evaluation metrics	Standard wall function	Literature models	Wall function ( $\psi$ )
RMSE	0.148	0.167	0.042
ME	0.520	0.400	0.230
$R^2$	0.853	0.949	0.985

displays anisotropy, making the RSM a preferable choice over the  $k-\epsilon$  model. Nonetheless, in the majority of scenarios, the  $k-\epsilon$  model exhibits superior performance while maintaining computational efficiency.

Finally, it is essential to acknowledge the limitations and gaps identified within our current study. The experimental data employed in this research, sourced from Dash,<sup>38</sup> rely on the ultrasound imaging velocimetry (UIV) technique utilizing a medical ultrasound device. The UIV method captures acoustic signals through transducers, which exhibit significant variance with respect to depth, thus introducing limitations in penetration. We intend to address this concern by utilizing a dedicated ultrasonic velocity profiler (UVP) in forthcoming publications. It is important to note that, despite using particles significantly smaller than the threshold, settling phenomena were observed in cases with lower velocities, complicating our ability to draw definitive conclusions. Additionally, our assumption of a homogeneous particle–fluid mixture neglects the influences of Brownian motion and gravity, leading to non-homogeneity. While a two-phase CFD model can address these challenges, it necessitates a trade-off in computational cost due to the requirement for finer mesh, additional transport equations, and advanced solver settings. These considerations underscore the intricate balance between model accuracy and computational efficiency.

These limitations and gaps provide avenues for future research and call for further exploration and refinement of the proposed modeling approach to improve accuracy and address the complexities associated with non-Newtonian fluid flows.

## ACKNOWLEDGMENTS

This article is the result of research conducted and funded by the Department of Water Management at Delft University of Technology, the Netherlands. We want to thank Professor C. Poelma and A. Dash from the Process & Energy Department at Delft University of Technology, the Netherlands, for sharing their experimental data, which greatly contributed to this article.

## AUTHOR DECLARATIONS

### Conflict of Interest

The authors have no conflicts to disclose.

### Author Contributions

**Bilal Khan Yusufi:** Conceptualization (lead); Formal analysis (lead); Investigation (lead); Methodology (lead); Validation (lead); Visualization (lead); Writing—original draft (lead); Writing—review & editing (equal). **Zoran Kapelan:** Project administration (equal); Supervision (equal); Writing—review & editing (equal). **Dhruv Mehta:** Conceptualization (equal); Methodology (equal); Project administration (lead); Resources (lead); Supervision (lead); Writing—review & editing (equal).

## DATA AVAILABILITY

The experimental data used in this research article were provided by the original author (Dash, 2022) upon request and are openly accessible within the TU Delft repository via the following link: <https://doi.org/10.4233/uuid:f62e9c3c-934f-425a-870f-84b8f56f104e>.

The wall function codes, mesh files, and scripts used to generate the figures in this article have been deposited in a GitHub repository available at [https://github.com/bilalkh119/POF\\_2023\\_B.Yusufi](https://github.com/bilalkh119/POF_2023_B.Yusufi).

## REFERENCES

- Y. Tomita, “A study on non-Newtonian flow in pipe lines,” *Bull. JSME* **2**, 10–16 (1959).
- L. Prandtl, “Ueber die ausgebildete Turbulenz,” in *Proceedings of the Second International Congress for Applied Mechanics, Zurich, September 1926* (Orell Fussli Verlag, Zurich, 1927), p. 62.
- D. W. Dodge and A. B. Metzner, “Turbulent flow of non-Newtonian systems,” *AIChE J.* **5**, 189–204 (1959).
- E. Buckingham, “On physically similar systems; illustrations of the use of dimensional equations,” *Phys. Rev.* **4**, 345–376 (1914).
- B. M. Torrance, “Friction factors for turbulent non-Newtonian fluid flow in circular pipes,” *South Afr. Mech. Eng.* **13**, 89–91 (1963).
- K. C. Wilson and A. D. Thomas, “A new analysis of the turbulent flow of non-Newtonian fluids,” *Can. J. Chem. Eng.* **63**, 539–546 (1985).
- A. D. Thomas and K. C. Wilson, “New analysis of non-Newtonian turbulent flow—yield-power-law fluids,” *Can. J. Chem. Eng.* **65**, 335–338 (1987).
- P. T. Slatter, “Modelling the turbulent flow of non-Newtonian slurries,” *R D J.* **12**, 68 (1996).
- R. Chhabra and J. Richardson, “Flow in pipes and in conduits of non-circular cross-sections,” in *Non-Newtonian Flow and Applied Rheology* (Butterworth-Heinemann, Oxford, 2008), Ch. 110–205, pp. 335–338, ISBN 9780750685320.
- A. Szilas, E. Bobok, and L. Navratil, “Determination of turbulent pressure loss of non-newtonian oil flow in rough pipes,” *Rheol. Acta* **20**, 487–496 (1981).
- R. L. Bowen, “Designing turbulent-flow systems,” *Chem. Eng.* **68**, 143 (1961).
- J. Peixinho, C. Nouar, C. Desaubry, and B. Théron, “Laminar transitional and turbulent flow of yield stress fluid in a pipe,” *J. Non-Newtonian Fluid Mech.* **128**, 172 (2005).
- N. I. Heywood and D. C. Cheng, “Comparison of methods for predicting head loss in turbulent pipe flow of non-Newtonian fluids,” *Trans. Inst. Meas. Control* **6**, 33 (1984).
- R. W. Hanks, “Low Reynolds number turbulent pipeline flow of pseudohomogeneous slurries,” in *Hydrotransport 5, Papers Presented at the Fifth International Conference on the Hydraulic Transport of Solids in Pipes, Hannover, Germany, 8–11 May 1978* (BHRA Fluid Engineering, 1978), pp. 22–34.
- S. M. Paker, Ş. Helvacı, H. B. Yener, B. İkizler, and A. Alparslan, *Solid-Liquid Two Phase Flow* (Elsevier, Amsterdam, 2008), pp. 1–70.
- K. M. Assefa and D. R. Kaushal, “A comparative study of friction factor correlations for high concentrate slurry flow in smooth pipes,” *J. Hydrol. Hydromech.* **63**, 13–20 (2015).
- M. Rudman and H. Blackburn, “Direct numerical simulation of turbulent non-Newtonian flow using a spectral element method,” *Appl. Math. Modell.* **30**, 1229–1248 (2006).
- F. T. Pinho, “A GNF framework for turbulent flow models of drag reducing fluids and proposal for a  $k-\epsilon$  type closure,” *J. Non-Newtonian Fluid Mech.* **114**, 149–184 (2003).
- K. Hanjalic, “Will RANS survive LES? A view of perspectives,” *J. Fluids Eng.* **127**, 831–839 (2005).
- S. Lovato, G. Keetels, S. Toxopeus, and J. Settels, “An eddy-viscosity model for turbulent flows of Herschel–Bulkley fluids,” *J. Non-Newtonian Fluid Mech.* **301**, 104729 (2022).
- P. A. Davidson, “The origins and nature of turbulence,” in *Turbulence: An Introduction for Scientists and Engineers* (Oxford University Press, 2015), Ch. 3, pp. 61–104.
- P. Spalart and S. Allmaras, “A one-equation turbulence model for aerodynamic flows,” AIAA Paper No. 1992-0439, 1992.
- B. Launder and D. Spalding, “The numerical computation of turbulent flows,” *Comput. Methods Appl. Mech. Eng.* **3**, 269–289 (1974).
- D. C. Wilcox, “Reassessment of the scale-determining equation for advanced turbulence models,” *AIAA J.* **26**, 1299 (1988).
- B. E. Launder, G. J. Reece, and W. Rodi, “Progress in the development of a Reynolds-stress turbulence closure,” *J. Fluid Mech.* **68**, 537–566 (1975).

- <sup>26</sup>D. C. Wilcox, "One-equation and two-equation models," in *Turbulence Modeling for CFD*, 3rd ed. (DCW Industries, 2006), Ch. 4, pp. 107–238.
- <sup>27</sup>M. Malin, "The turbulent flow of Bingham plastic fluids in smooth circular tubes," *Int. Commun. Heat Mass Transfer* **24**, 793–804 (1997).
- <sup>28</sup>M. Malin, "Turbulent pipe flow of Herschel–Bulkley fluids," *Int. Commun. Heat Mass Transfer* **25**, 321–330 (1998).
- <sup>29</sup>M. Malin, "Turbulent pipe flow of power-law fluids," *Int. Commun. Heat Mass Transfer* **24**, 977–988 (1997).
- <sup>30</sup>A. Bartosik, "Application of rheological models in prediction of turbulent slurry flow," *Flow. Turbul. Combust.* **84**, 277–293 (2010).
- <sup>31</sup>D. Cruz and F. Pinho, "Turbulent pipe flow predictions with a low Reynolds number  $k-\epsilon$  model for drag reducing fluids," *J. Non-Newtonian Fluid Mech.* **114**, 109–148 (2003).
- <sup>32</sup>D. Cruz, F. Pinho, and P. Resende, "Modelling the new stress for improved drag reduction predictions of viscoelastic pipe flow," *J. Non-Newtonian Fluid Mech.* **121**, 127–141 (2004).
- <sup>33</sup>A. A. Gavrilov and V. Y. Rudyak, "Reynolds-averaged modeling of turbulent flows of power-law fluids," *J. Non-Newtonian Fluid Mech.* **227**, 45–55 (2016).
- <sup>34</sup>A. Gavrilov and V. Rudyak, "A model of averaged molecular viscosity for turbulent flow of non-Newtonian fluids," *J. Sib. Fed. Univ., Math. Phys.* **7**, 46–57 (2014).
- <sup>35</sup>R. Sawko, "Mathematical and computational methods of Non-Newtonian, multiphase flows," Ph.D. thesis, Cranfield University, 2012.
- <sup>36</sup>R. Clapp, "Turbulent heat transfer in pseudoplastic non-Newtonian fluids," in *International Developments of Heat Transfer Part III* (The American Society of Mechanical Engineers, New York, NY, USA, 1961), pp. 652–661.
- <sup>37</sup>D. Mehta, A. Thota Radhakrishnan, J. Van Lier, and F. Clemens, "A wall boundary condition for the simulation of a turbulent non-Newtonian domestic slurry in pipes," *Water* **10**, 124 (2018).
- <sup>38</sup>A. Dash, "Opaque inertial suspensions," Ph.D. thesis, Delft University of Technology, 2022.
- <sup>39</sup>W. Herschel and R. Bulkley, "Consistency measurements of gum-benzene solutions," *Colloid J.* **39**, 291–300 (1926).
- <sup>40</sup>J. G. Oldroyd, "A rational formulation of the equations of plastic flow for a Bingham solid," *Math. Proc. Cambridge Philos. Soc.* **43**, 100–105 (1947).
- <sup>41</sup>M. Rudman, H. Blackburn, L. Graham, and L. Pullum, "Turbulent pipe flow of shear-thinning fluids," *J. Non-Newtonian Fluid Mech.* **118**, 33–48 (2004).
- <sup>42</sup>A. B. Metzner and J. C. Reed, "Flow of non-Newtonian fluids-correlation of the laminar, transition, and turbulent-flow regions," *AIChE J.* **1**, 434–440 (1955).
- <sup>43</sup>A. A. Aliabadi, "Wall models," in *Turbulence: A Fundamental Approach for Scientists and Engineers* (Springer Nature Switzerland AG, 2022), pp. 235–250.
- <sup>44</sup>J. H. Ferziger, M. Perić, and R. L. Street, "Turbulent flows," in *Computational Methods for Fluid Dynamics* (Springer Nature Switzerland AG, 2020), pp. 347–419.
- <sup>45</sup>D. Mehta, A. T. Radhakrishnan, J. V. Lier, and F. Clemens, "Sensitivity analysis of a wall boundary condition for the turbulent pipe flow of Herschel–Bulkley fluids," *Water* **11**, 19 (2018).
- <sup>46</sup>ANSYS, Inc. *Ansys Fluent Theory Guide*, Release 2021 R2 ed., ANSYS, Inc., 2021.
- <sup>47</sup>A. Dash, W. Hogendoorn, G. Oldenziel, and C. Poelma, "Ultrasound imaging velocimetry in particle-laden flows: Counteracting attenuation with correlation averaging" *Exp. Fluids* **63**(3), 56 (2022).
- <sup>48</sup>A. Dash and C. Poelma, "Long-time-scale transients in an industrial-scale slurry pipeline near the laminar-turbulent transition" *Flow* **2**, E25 (2022).
- <sup>49</sup>A. T. Radhakrishnan, "Domestic slurry hydraulics in transport," Doctoral thesis, Delft University of Technology, 2019.
- <sup>50</sup>G. V. Messa, Q. Yang, O. E. Adedeji, Z. Chára, C. A. R. Duarte, V. Matoušek, M. G. Rasteiro, R. S. Sanders, R. C. Silva, and F. J. de Souza, "Computational fluid dynamics modelling of liquid-solid slurry flows in pipelines: State-of-the-art and future perspectives," *Processes* **9**, 1566 (2021).
- <sup>51</sup>T. D. Reed and A. A. Pilehvari, "A new model for laminar, transitional, and turbulent flow of drilling muds," in SPE Production Operations Symposium, Oklahoma City, Oklahoma, 1993.
- <sup>52</sup>M. Escudier and F. Presti, "Pipe flow of a thixotropic liquid," *J. Non-Newtonian Fluid Mech.* **62**, 291–306 (1996).
- <sup>53</sup>B. O. A. Hedstrom, "Flow of plastics materials in pipes," *Ind. Eng. Chem.* **44**, 651 (1952).
- <sup>54</sup>R. W. Hanks, "The laminar-turbulent transition for fluids with a yield stress," *AIChE J.* **9**, 306–309 (1963).
- <sup>55</sup>P. Dutta, S. K. Saha, N. Nandi, and N. Pal, "Numerical study on flow separation in 90° pipe bend under high Reynolds number by  $k-\epsilon$  modelling," *Eng. Sci. Technol., an Int. J.* **19**, 904–910 (2016).
- <sup>56</sup>C. Carlsson, E. Alenius, and L. Fuchs, "Swirl switching in turbulent flow through 90° pipe bends," *Phys. Fluids* **27**, 085112 (2015).
- <sup>57</sup>K. Sudo, M. Sumida, and H. Hibara, "Experimental investigation on turbulent flow in a circular-sectioned 90° bend," *Exp. Fluids* **25**, 42–49 (1998).
- <sup>58</sup>E. Zheng, M. Rudman, S. Kuang, and A. Chryss, "Turbulent coarse-particle suspension flow: Measurement and modelling," *Powder Technol.* **373**, 647–659 (2020).
- <sup>59</sup>E. J. Wasp, "Slurry pipelines," *Sci. Am.* **249**, 48–55 (1983).
- <sup>60</sup>A. Kalpakli and R. Örlü, "Turbulent pipe flow downstream a 90° pipe bend with and without superimposed swirl," *Int. J. Heat Fluid Flow* **41**, 103–111 (2013).
- <sup>61</sup>D. Mehta, A. K. Thota Radhakrishnan, J. B. van Lier, and F. H. Clemens, "Assessment of numerical methods for estimating the wall shear stress in turbulent Herschel–Bulkley slurries in circular pipes," *J. Hydraul. Res.* **59**, 196–213 (2021).